Bimodal Electrochemiluminescence Microscopy of Single Cells

# Multimodal Electrochemiluminescence Microscopy of Single Cells

Sara Knežević,[a] Emily Kerr,[b] Bertrand Goudeau,[a] Giovanni Valenti,[c] Francesco Paolucci,[c] Paul S. Francis,[d] Frédéric Kanoufi,[e] Neso Sojic*,[a]

Electrochemiluminescence (ECL) microscopy is an emerging technique with new applications such as the imaging of single entities and cells. Herein, we have developed a multimodal and multicolor approach to record both positive ECL (PECL: light-emitting object on dark background) and shadow label-free ECL (SECL: non-emissive object shadowing the background luminescence) images of single cells. This multimodal approach is the result of the simultaneous emissions of $[Ru(bpy)_3]^{2+}$ used to label the cellular membrane (PECL) and $[Ir(sppy)_3]^{3-}$ dissolved in solution (SECL). By spectrally resolving the ECL emission wavelengths, we recorded the images of the same cells in both PECL and SECL modes using the $[Ru(bpy)_3]^{2+}$ ($\lambda_{max}$ = 620 nm) and $[Ir(sppy)_3]^{3-}$ ($\lambda_{max}$ = 515 nm) luminescence, respectively. PECL shows the distribution of the $[Ru(bpy)_3]^{2+}$ labels attached to the cellular membrane whereas SECL reflects the local diffusional hindrance of the ECL reagents by each cell. The high sensitivity and surface-confined features of the reported approach is demonstrated by imaging cell-cell contacts during the mitosis process. Furthermore, the comparison of PECL and SECL images demonstrates the differential diffusion of tri-*n*-propylamine and $[Ir(sppy)_3]^{3-}$ through the permeabilized cell membranes. Consequently, this dual approach enables the imaging of the morphology of the cell adhering on the surface and can significantly contribute to multimodal ECL imaging and bioassays with different luminescent systems.

## Introduction

Electrochemiluminescence (ECL) is a phenomenon that occurs when the energy released in an electrochemically triggered redox reaction forms an excited electronic state of the luminophore, which in turn emits light.[1] As an electrochemical method with an optical output, ECL possesses high sensitivity, spatial and temporal resolutions, and near zero background, distinguishing it from purely electrochemical or photoluminescent (PL) methods. Recently, researchers have combined ECL with modern microscopy techniques to examine ECL of single entities,[2–4] dynamic events,[5] collisions,[6–9] mechanistic pathways underpinning ECL,[10–13] catalytic activity,[14–16] reactions occurring at phase interfaces,[17–19] biological assays[20,21] and the investigation of biological systems and processes (cells, organelles, proteins, membrane transport properties).[22–24]

Generally, a redox reaction between a luminophore and a sacrificial co-reactant, triggered by an applied potential, is essential for ECL generation in aqueous environments. The model ECL system consists of tris(2,2'-bipyridine)ruthenium(II) ($[Ru(bpy)_3]^{2+}$) and tri-*n*-propylamine (TPrA), as luminophore and co-reactant, respectively.[25,26] This system has been extensively studied and employed in the ECL imaging of single objects (including cells and proteins) in two experimental configurations: (i) 'positive'[4,14,23,27–30] and (ii) 'shadow' or 'negative'.[31–34] In positive ECL (PECL) microscopy configurations, the imaged object is either electroactive itself and can directly generate ECL[28,35] or it is labelled with an ECL-active luminophore.[10,36] In this later case, after application of an appropriate electrochemical potential, the luminophore undergoes a cascade of redox reactions with electrogenerated TPrA radicals (Scheme 1B and Fig. S1) to form the excited state that generates light upon decay.[26] The emitted light is confined to the labelled object, in the immediate vicinity of the electrode surface, resulting in the image of a bright labelled object against a dark background. Conversely, in shadow ECL (SECL) microscopy configurations, both the luminophore and co-reactant are freely diffusing in the solution. After electrochemical oxidation, these species can interact to form the excited state of the luminophore (Scheme 1C). In the SECL configuration, the objects to be imaged (e.g., cells) are deposited on the electrode surface. When an electrochemical potential is applied to the electrode, luminescence is seen over the entire electrode surface, except in regions where the imaged object is present.[34] In such regions, diffusional flux of the luminophore and/or co-reactant towards the electrode surface is hindered, thus blocking the electrochemical reactions necessary to produce ECL in these regions. SECL is a label-free method, which results in an image of a dark object against a bright background.

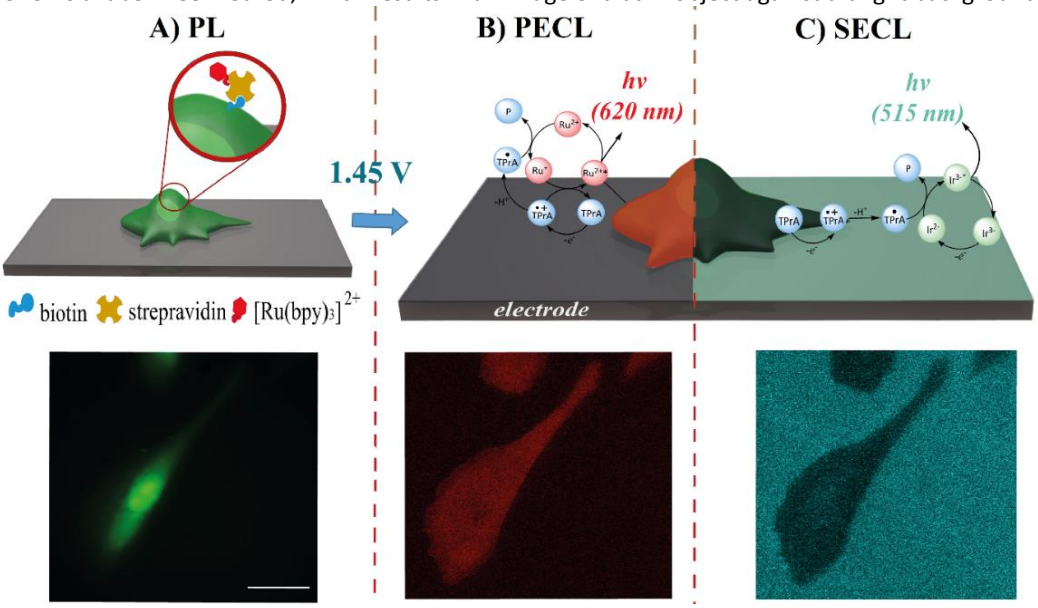


**Scheme 1.** (Top) Schematic representation of multimodal imaging of a cell immobilized on a glassy carbon electrode (GCE): (A) PL, (B) PECL and (C) SECL. Mechanisms of co-reactant PECL (heterogeneous route involving mainly dissolved TPrA and SA@Ru label immobilized on the cell) and SECL (homogeneous route involving only dissolved $[Ir(sppy)_3]^{3-}$ and TPrA) modes. $Ru^{2+}$ and $Ir^{3-}$ represent the ECL SA@Ru-label and $[Ir(sppy)_3]^{3-}$, respectively. (Bottom) The same single CHO-K1 cell was visualized by (A) PL, (B) PECL and (C) SECL. Different filters sets were used to acquire PL, PECL and SECL images (Fig. S2). Scale bar: 30 µm.

Both PECL and SECL have been used extensively in ECL imaging.[37] For example, labelling the cellular membrane proteins with $[Ru(bpy)_3]^{2+}$ allows one to image the expression of proteins, membrane transport properties and processes occurring in the vicinity of the electrode surface using PECL.[12,27,36,38,39] The diagnostic application of this approach was demonstrated by labelling a plasma receptor overexpressed in tumor cells.[38] The spatial confinement of ECL could be tuned with different experimental strategies[10,11,32,40] and is mainly controlled by the short half-lives of electrogenerated TPrA radicals that react with the

luminophore, enabling formation of the excited state. The main downside of PECL is the relatively low luminescence intensity, a consequence of the limited number of molecular luminophores attached as labels,[27,36] even if ECL-active nanoparticles may be used to detect single biomolecules.[38,41] The emission intensity further decreases with each applied chronoamperometric pulse due to depletion of co-reactant in the diffusion layer and surface passivation of the electrode, but slightly improves after cathodic surface regeneration treatment.[42] Attempts to perform ultrasensitive ECL analysis, which would enable single-protein detection, required the use of $[Ru(bpy)_3]^{2+}$-doped silica/Au nanoparticle (nanoemitter)-labelled antibodies that can bind to membrane proteins and enhance the intensity of Ru-derived ECL in the presence of TPrA.[38]

Studying cellular heterogeneity using a negative signal from the unlabeled cell hindering the diffusion of luminophore and co-reactant to the electrode surface – SECL – has been applied to the study of single cells with remarkable spatial resolution,[33] cell-matrix adhesions,[24] morphological changes under oxidative stress,[43] migration of living cells[24] and imaging mitochondria.[34] Furthermore, by varying the concentration of freely diffusing luminophore, it is possible to extend the otherwise electrode surface confined ECL layer in order to image cell-cell junctions[32] and upper cell membranes.[44] This approach not only gives information on the cell shape and dynamic processes of the cellular adhesions but also can spatially resolve objects along the z-axis, which is not easily achievable using PECL. In addition, SECL microscopy can allow investigation of the transport properties through membranes. However, since SECL is a label-free approach, it can neither distinguish processes occurring on or inside the cellular membrane nor discriminate the proteins or different biological factors in diverse cells. Thus, these two ECL modes are considered complementary, and their combination can give a variety of information on the structure-function properties and processes that occur in the observed system.

To develop multimodal ECL combining SECL and PECL, we need to resolve – spectrally, potentiometrically, and/or spatially – ECL emitted by a luminophore in solution-phase from ECL produced by a luminophore that is immobilized on a cell membrane. This can be achieved by introducing an additional luminophore to the $[Ru(bpy)_3]^{2+}$/TPrA system. This second luminophore must emit light at a wavelength distinct from that of $[Ru(bpy)_3]^{2+}$ ($\lambda_{max}$ = 620 nm) to facilitate spectral resolution of the emission from the two luminophores (Fig. S2). In recent years, Ir(III) complexes have emerged as promising alternatives to traditional Ru(II) luminophores for analytical applications of ECL sensing. Ir(III) complexes emit bright ECL with TPrA as a co-reactant and exhibit ECL emissions into the blue region of the visible spectrum.[45–56] Furthermore, extensive research into multiplexed ECL systems – examining combinations of Ru(II) and Ir(III) metal chelates – has already demonstrated the ability to potentiometrically and/or spectrally resolve the ECL emissions from solutions containing combinations of such complexes.[57–63] Therefore, Ir(III) emitters are ideal candidates as the secondary luminophore in a combined SECL and PECL imaging strategy. Recently, Kerr et al. used a novel green-emissive ($\lambda_{max}$ = 515 nm, Fig. S2) water-soluble complex, $[Ir(sppy)_3]^{3-}$ (sppy = 5′-sulfo-2-phenylpyridinato-$C^2$,$N$), in a mixed solution-phase ECL system with $[Ru(bpy)_3]^{2+}$ and TPrA co-reactant.[64] The researchers were able to spectrally distinguish the ECL emissions from the two complexes, but also found that the $[Ir(sppy)_3]^{3-}$ complex enhanced ECL from the $[Ru(bpy)_3]^{2+}$ in the homogeneous phase by more than an order of magnitude.[64]

In this work, we used $[Ru(bpy)_3]^{2+}$-labelled CHO-K1 cells in the presence of dissolved $[Ir(sppy)_3]^{3-}$ luminophore and TPrA co-reactant (**Scheme 1**) to achieve simultaneous SECL and PECL microscopy from the same cell. A novel, multimodal and multicolor ECL approach is demonstrated for cell imaging. PECL microscopy reflects the distribution of the $[Ru(bpy)_3]^{2+}$ labels (denoted SA@Ru) whereas SECL is the negative signature of the diffusion hindered by the cell membranes. Combining both PECL and SECL images gives insight into the transport properties of TPrA and $[Ir(sppy)_3]^{3-}$ through the permeabilized cell membranes.

## Results and discussion

In developing a multimodal ECL imaging approach, the adherent CHO-K1 cells were grown on the GCE surface. The cells were permeabilized with Triton X-100 as classically performed in immunofluorescence or Western blot methods.[36,65,66] The SA@Ru labels were attached to membrane proteins using the well-known streptavidin-biotin interactions. Biotin unselectively binds to the primary amino groups of membrane proteins, which enabled attachment of the SA@Ru to the entire cell membrane. This type of labelling was chosen as a proof-of-concept approach to demonstrate the complementarity of information obtained in two ECL modes – SECL and PECL – and the applicability of SA@Ru (PECL) and $[Ir(sppy)_3]^{3-}$ (SECL) emissions to image distinct features, that may be difficult to observe using traditional PL imaging strategies (primarily the morphology of the cell, cell-surface adhesions, cell-cell junctions transport and transport through the permeabilized membrane). The electrodes decorated with cells were immersed in a custom-made electrochemical cell suitable for microscopy, containing 100 µM $[Ir(sppy)_3]^{3-}$ in a commercially available ProCell buffer solution (0.18 M TPrA). Two distinct sets of experiments were performed to demonstrate the properties of this approach: multimodal ECL imaging and study of the ability of $[Ir(sppy)_3]^{3-}$ to give a more stable luminescence from $[Ru(bpy)_3]^{2+}$ labels (i.e. SA@Ru) during the recording of successive ECL images.

In a first set of experiments, we used a wide-field microscope to obtain a PL image of the cells immobilized on the non-transparent GCE surface in a reflection mode and through the solution (Scheme 1A and Fig. 1A). For the PL microscopy, a filter set suitable to detect the emission from the $[Ru(bpy)_3]^{2+}$ luminophore was chosen. In other words, PL images show the SA@Ru labelling sites on the whole surface of the cellular membrane, proving that there are no unlabeled regions. The background PL signal, already high due to the autoluminescence and the excitation light scattering by the non-transparent GCE surface, is increased owing to the presence of the $[Ir(sppy)_3]^{3-}$ luminophore in the solution. Turning off the excitation light and applying a constant 1.45 V potential pulse resulted in ECL imaging of the identical location with the $[Ru(bpy)_3]^{2+}$ and $[Ir(sppy)_3]^{3-}$ complexes. The luminescence of the two can be discriminated using suitable bandpass emission filters (Fig. S2) to create two complementary ECL images: PECL derived from $[Ru(bpy)_3]^{2+*}$ (i.e. SA@Ru*) and SECL derived from $[Ir(sppy)_3]^{3-*}$ (Scheme 1 and Fig. 1). ECL emission of SA@Ru is initiated by the oxidation of TPrA. The resulting $TPrA^{\bullet+}$ radical deprotonates and forms the strongly reducing neutral $TPrA^{\bullet}$ radical. As illustrated by Scheme 1B, both radicals react sequentially with SA@Ru to produce its excited state at the level of the plasma membrane, leading *in fine* to the local ECL emission at 620 nm.[25,26,67] This mechanism follows the heterogeneous ECL route because the SA@Ru is immobilized on an insulating entity and cannot be directly oxidized at the electrode surface. It is also called the "revisited" or "remote" route.[26,67] Since the $[Ir(sppy)_3]^{3-}$ complex is present in solution, another mechanistic possibility for the generation of the excited state SA@Ru* can operate *via* the 'redox-mediator' route[64] (Fig. S1**)**. It has been demonstrated recently by Kerr et al. with both $[Ir(sppy)_3]^{3-}$ and $[Ru(bpy)_3]^{2+}$ complexes dissolved in solution but not for the heterogeneous format (i.e. $[Ru(bpy)_3]^{2+}$ immobilized and $[Ir(sppy)_3]^{3-}$ in solution). In this route, both TPrA and $[Ir(sppy)_3]^{3-}$ are oxidized directly at the electrode surface. The neutral $TPrA^{\bullet}$ radical reduces the label SA@Ru to the $[Ru(bpy)_3]^{+}$ state, which is oxidized by $[Ir(sppy)_3]^{2-}$ in a sufficiently exergonic reaction to produce the excited state SA@Ru*. Finally, the electrocatalytic route with the indirect oxidation of TPrA by the oxidized $[Ir(sppy)_3]^{2-}$ form may also occur (Scheme S1). In brief, these mechanisms (i.e. the revisited, redox-mediator[64] and electrocatalytic pathways) may occur with different prevalence in the case of PECL microscopy resulting in the emission at 620 nm. For SECL with light emission at 515 nm, the excited state $[Ir(sppy)_3]^{3-*}$ results from the oxidation of TPrA and $[Ir(sppy)_3]^{3-}$ at the electrode surface and their subsequent reaction in the homogeneous phase (Scheme 1C**)**. More complex mechanisms with competitive pathways are possible as well[26,64] whose investigation is however outside the scope of the present cell imaging study.

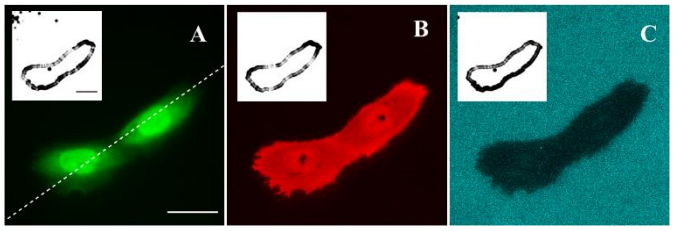


**Fig. 1**. (A) PL, (B) PECL (showing only SA@Ru ECL emission) and (C) SECL (showing only $[Ir(sppy)_3]^{3-}$ emission) micrographs of the same cells. The images are recorded in Procell with 100 µM $[Ir(sppy)_3]^{3-}$. Dotted line denotes a direction in which PL and ECL intensity profiles were extracted. Inset A: PL to SECL, inset B: PL to PECL, and inset C SECL to PECL difference SSIM maps. Scale bar: 30 µm.

Regardless, the ECL images enable visualization of a larger area of the plasma membrane in comparison to PL, showing finer membrane details and extended cellular structures such as different cell-electrode adhesions along the cell margin (Scheme 1). Similarly, Fig. 1 displays two cells during the mitosis process (i.e. cell division). The PECL image reveals the entire surface-confined area of the cells, in good agreement with the PL image, except the two dark regions in the middle of the nuclei. Since the PL mode clearly shows that the whole plasma membrane was labelled, these dark regions therefore do not indicate the absence of the luminophore but rather the local hindrance of the TPrA diffusion to the electrode, which effects the PECL but not the PL mode. As previously described in the literature,[36] the reason for this diffusional hindrance is the presence of nucleoli: RNA-producing structures in mammalian cell nuclei. These organelles have a membrane that is less susceptible to the influence of surfactants and to the permeabilization procedure. Thus, the nucleoli membrane remains unpermeabilized and blocks the co-reactant diffusion to the electrode surface, causing the appearance of dark regions.[36] As reported previously, TPrA can diffuse through the permeabilized plasma membrane allowing visualization of the cell by PECL.[36] Therefore, if the iridium complex cannot diffuse through the plasma membrane, the SECL image should ideally be the opposite image to the PECL one. From Fig. 1, we see that, except for the nucleoli, both ECL modes uncover the total area of the cells, but with inverted bright and dark regions. The comparison of both ECL modes (PECL *vs* SECL) indicates that the TPrA co-reactant can diffuse through the permeabilized plasma membrane (PECL), whereas diffusion of the $[Ir(sppy)_3]^{3-}$ complex is hindered in the reported experimental conditions. Indeed, on one hand, both cells are clearly visible in PECL indicating that TPrA can diffuse through the cell membranes.

On the other hand, the cells remain dark in SECL due to the blocking of the $[Ir(sppy)_3]^{3-}$ diffusion by the membrane. This is important because it demonstrates that the transport through the cell membranes of different molecules involved in the ECL process can be discriminated by combining SECL and PECL. While its size can contribute to the slower diffusion of the Ir(III) complex through the permeabilized cell membrane, other parameters may also affect transport through the cell membranes and thus the final SECL signal. Indeed, other iridium complexes have been successfully used for cell staining.[68–70] It was reported that the charge, amphiphilicity and protein binding characteristics of the iridium complexes are crucial for their distribution and staining performance.[68] Since the reported complexes are positively charged and have different polarity than the $[Ir(sppy)_3]^{3-}$ used in this study, they may have distinct transport properties through the net negatively charged cellular membrane and SECL microscopy could allow resolving this difference.

On Fig. 1, one can observe two cells at the last stage of the mitosis. The nuclei are well-separated, but the plasma membranes of each cell are not completely disconnected. In this region, the cell-cell contacts of the plasma membranes are visible in PL on Fig. 1A but with a low contrast. On the other hand, this thin inter-cell region of the plasma membranes is easily visualized by both PECL and SECL. It emits a strong ECL emission in PECL and remains completely dark in SECL. Indeed, ECL is a surface-confined process triggered by an initial electron-transfer reaction and this remaining cell-cell plasma region blocks the ECL process leading to strong positive or negative easy-detectable signals in both PECL and SECL modes, respectively.

To further confirm these observations and provide more details about the information revealed using different modes, we constructed structure similarity index measurement (SSIM) maps. SSIM maps depict morphological differences between images obtained using PL and SECL (Inset Fig. 1A), PL and PECL (Inset Fig. 1B) and SECL and PECL (Inset Fig. 1C), with SSIM indexes being 0.925, 0.94 and 0.91, respectively. These indexes are numbers scaled from 0 to 1, describing the level of similarity between the two images, with 1 being a perfect match. The high index values (above 0.9) obtained for all combinations of the images confirm that the areas displayed on all of them are the same, with the distinct regions on the cell periphery indicating the above-mentioned differences in the ability of PL and ECL to resolve fine structural details and disparities of the thin cell-electrode adhesions and cell-cell junctions. Furthermore, SSIM difference maps for PL/SECL and PECL/SECL show several pixels near the edge of the image and one on the top border of the cell. This difference is due to slight variations in the SSIM map generation process. Namely, to create the maps, it is necessary to threshold the original microscopic images and to condense the total information about the intensities of pixels to only two: black and white. Consequently, depending on the contrast and the occurrence of incidentally brighter/darker pixels in each mode, the chosen threshold will not be identical, additionally contributing to the differences in the ISSM maps and indexes.

To investigate further the PL/ECL imaging capabilities, we extracted the PL and ECL profiles (Fig. 2) along the section indicated by a dotted line in Fig. 1A. The intensity of the PL profiles is lowest at the periphery of the cells, increases in the proximity of the nuclei and reaches two distinct maxima at the nuclei centers. In PL mode, both $[Ru(bpy)_3]^{2+}$ and $[Ir(sppy)_3]^{3-}$ are excited and emissions from the two luminophores is observed simultaneously. Absorption and emission spectra of the complexes overlaid with FITC/LP filter cube's excitation, dichroic and suppression filter cutoffs are given in Fig. S2B. Considering that the luminophores at the whole surface of cell membrane are excited simultaneously, the thicker regions that contain more labels appear brighter in the PL image. Because ECL is confined to a region close to the electrode surface (due to the short lifetimes of TPrA radicals), the focal plane of ECL is closer to the electrode surface relative to PL.[36] Due to this confinement, in a first order approximation, we do not expect to observe differences in ECL intensity in the regions that have different thicknesses. Indeed, PECL and SECL profiles look like mirror images of each other, showing the outline of the basal cell membrane without discriminating the areas based on the thickness of the membrane or cell-cell junctions (Fig. 2). Furthermore, dark spots visible in the centers of the nuclei in the PECL image in Fig. 1C can be seen in the PECL profile as slight drops in intensity, confirming that co-reactant diffusion is hindered but not completely blocked in these regions. As a visual confirmation of described differences between PL, SECL and PECL, 3D intensity profiles were extracted (Fig. S3) and depict the variation in PL and ECL intensities over the whole surface of the cells. The similarities in the PECL and SECL patterns – considered positively or negatively – may indicate that the same part of the cell is imaged in the reported experimental conditions. It points to the probable dominant role of the lifetime of the TPrA cation radicals, which determines the ECL-layer thickness in both ECL processes. Tuning the ECL-layer thickness by changing the respective concentrations of TPrA and $[Ir(sppy)_3]^{3-}$, or even the co-reactant itself, constitute an appealing future alternative, as demonstrated previously for the $[Ru(bpy)_3]^{2+}$ luminophore.[11,32]

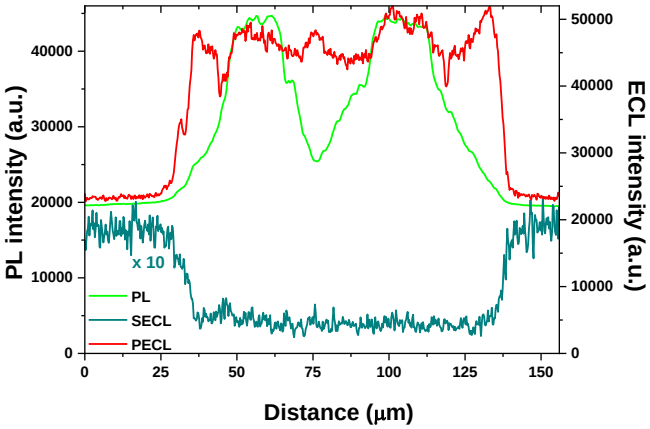


**Fig. 2**. PL, SECL and PECL intensity profiles of the cells extracted along the dashed line on Fig. 1A.

Despite being a luminophore with a high quantum yield ($\phi$ = 0.73),[71] $[Ir(sppy)_3]^{3-}$ exhibits weak ECL intensity with TPrA when compared to $[Ru(bpy)_3]^{2+}$ due to poor energetics with the TPrA co-reactant.[64] This results in SECL intensity being lower than PECL intensity by over an order of magnitude, which could be improved by examining alternative Ir(III) complexes that retain all the benefits of $[Ir(sppy)_3]^{3-}$ but generate more intense ECL with TPrA.[48,51,53,72]

The other set of experiments was designed to follow the trend in PECL intensity over eight subsequent potential pulses, with regeneration performed after the fifth pulse. A constant potential of 1.45 V for 5 s was used to generate the ECL signal. A distinct decrease was observed in the PECL signal with subsequent pulses (Fig. 3). This trend has been observed previously and results from passivation of the electrode surface by electro-oxidized TPrA. To counteract this, Han et al. developed an electrode surface regeneration procedure, consisting of 30 consecutive 1 s pulses to -1.8 V.[42] This regeneration procedure aims to concentrate the co-reactant in the vicinity of the electrode and to remove the passivating layer that can form on the electrode surface.[42] The PECL intensities were compared for the SA@Ru-labelled cells in ProCell solution and labelled cells in ProCell with 100 μM $[Ir(sppy)_3]^{3-}$. The results were averaged across sixteen electrodes for each solution. The experiments were performed during the course of two weeks at different temperature conditions (from 21°C to 42°C), storage times of the labelled cells, and periods in the day to make sure that the results are not biased due to external conditions. All intensities were determined as maximum intensities of background subtracted PECL profiles (described in the experimental section) and then averaged for each pulse independently over 16 electrodes to obtain the histogram in Fig. 3.

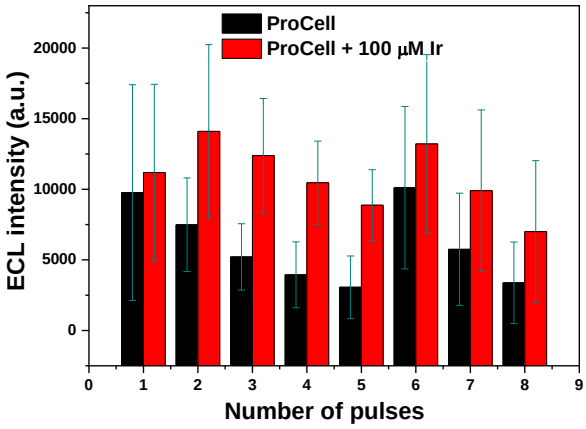


**Fig. 3**. PECL intensities averaged independently for 8 subsequent chronoamperometric pulses (regeneration performed after 5th pulse) over 16 different electrodes for the system containing 100 μM $[Ir(sppy)_3]^{3-}$ in ProCell buffer solution (red) and only ProCell buffer solution (black); error bars are set to ±1 value of the standard deviation of the ECL signal.

The error bars on the histogram represents ± 1 value of standard deviation and indicate high variability between different samples. This is a consequence of two combined effects: (i) the aforementioned variability due to change in external conditions and (ii) the high natural heterogeneity of the cultured cells. While the storage times and period in the day did not result in any observable change in average ECL intensities, the increase in temperature resulted in a slight increase in PECL for both systems. However, this increase is not statistically significant and is not a valid reason to omit any data points from the set. Also, cell shape and size proved to be important factors influencing the PECL intensities, thus significantly affecting the distribution of data points and introducing the high standard deviation in ECL values for the biological system. Thus, we conclude that this standard deviation depicts the heterogeneity of the cultured cells. Despite the high variability of the analysis, the histogram indicates that the intensities across all pulses are comparable or slightly higher for the system containing 100 µM $[Ir(sppy)_3]^{3-}$ in ProCell. Furthermore, PECL intensities decrease less with subsequent potential pulses and do not drastically increase after regeneration when the $[Ir(sppy)_3]^{3-}$ complex is present. This means $[Ru(bpy)_3]^{2+}$ ECL is more reproducible over several subsequent pulses when $[Ir(sppy)_3]^{3-}$ is present. However, at this stage, it is unclear how the presence of the dissolved $[Ir(sppy)_3]^{3-}$ complex allows avoiding the electrode passivation during successive ECL pulses. This is the first observation of the dual benefit of both enhanced reproducibility and ECL signal from $[Ru(bpy)_3]^{2+}$ in the bimodal $[Ru(bpy)_3]^{2+}/[Ir(sppy)_3]^{3-}$ system.

## Conclusions

In this paper, we demonstrate a new approach in ECL microscopy – multimodal and multicolor ECL – by exploiting the simultaneous ECL emissions of $[Ru(bpy)_3]^{2+}$ and $[Ir(sppy)_3]^{3-}$. Because $[Ru(bpy)_3]^{2+}$ is used to label the cells and $[Ir(sppy)_3]^{3-}$ is dissolved in solution their signals can be spatially resolved, while their distinct emission wavelengths (620 nm and 515 nm, respectively) enable simple spectral resolution by applying suitable emission filters to obtain micrographs in two modes: PECL (for $[Ru(bpy)_3]^{2+}$ emission) and SECL (for $[Ir(sppy)_3]^{3-}$ emission). Both images depict the same region of interest with the same cell, but regions emit opposite ECL intensity at different wavelengths. In this way, the reported approach provides complementary information about the observed system. On the one hand, PECL imaging shows the distribution of the SA@Ru labels on the cell membrane. On the other hand, SECL reflects the diffusional hindrance of the ECL reagents by the cell membranes. Comparing both images, we show that TPrA is able to diffuse through the permeabilized plasma membranes whereas diffusion of a larger $[Ir(sppy)_3]^{3-}$ molecule is blocked. After proving the feasibility of the multimodal approach, we confirmed that the presence of $[Ir(sppy)_3]^{3-}$ improves the reproducibility of the ECL microscopy. However, due to the low co-reactant ECL efficiency of $[Ir(sppy)_3]^{3-}$, the intensity of the SECL signal is comparatively low. Replacing this luminophore with similar Ir(III) complexes that give higher ECL intensity would improve contrast in SECL mode. This innovation in ECL imaging opens prospects in imaging distinct proteins or cellular structures, membrane transport properties, or single molecules at the cellular membrane using enhanced PECL, while simultaneously observing the outline of the cell and its morphological changes using SECL. The multimodal approach possesses numerous advantages when compared to traditional imaging techniques and could contribute not only to ECL microscopy but also to the development of more sensitive and reproducible ECL bioassays. Both PECL and SECL modes alleviate issues of photobleaching and phototoxicity associated with classical microscopy techniques. Furthermore, because it provides more information about the imaged objects, this approach could contribute to the fundamental studies of different biological systems, processes and reactions using bimodal ECL imaging.

## Author Contributions

**S.K.**: Investigation, Methodology, Analysis, Imaging, Writing – original draft. **E.K.**: Investigation, Analysis, Writing, Funding acquisition. **B.G.**: Design of the experimental setup, Experiments on cells. **G.V.**: Analysis, Interpretation of the images, Writing. **F.P.:** Analysis, Interpretation of the images, Writing. **P.S.F.:** Conceptualization, Supervision, Writing. **F.K.**: Conceptualization, Interpretation of the data, Writing. **N.S.**: Conceptualization, Supervision, Funding acquisition, Writing.

## Conflicts of interest

The authors declare no competing financial interests.

## Acknowledgements

This work was supported by Agence Nationale de la Recherche (ELISE - ANR-21-CE42). E. K. gratefully acknowledges the National Health and Medical Research Council (NHMRC) of Australia (GNT1161573), the Victorian Endowment for Science Knowledge and Innovation (VESKI) Victoria Fellowship, the Science and Industry Endowment Fund (SIEF) and Australian Academy of Science (AAS) SIEF-AAS Fellowship. G. V. and F. P. also acknowledge support from Italian MIUR (PRIN 2017FJCPEX and PRIN-2020CBEYHC)

## References


1 Z. Liu, W. Qi and G. Xu, *Chem. Soc. Rev.*, 2015, **44**, 3117–3142.
2 W. Zhao, H.-Y. Chen and J.-J. Xu, *Chem. Sci.*, 2021, **12**, 5720–5736.
3 J. Feng, *Curr. Opin. Electrochem.*, 2022, **34**, 101000.
4 J. Dong, Y. Xu, Z. Zhang and J. Feng, *Angew. Chem. Int. Ed.*, 2022, **61**, e202200187.
5 S. Knezevic, L. Bouffier, B. Liu, D. Jiang and N. Sojic, *Curr. Opin. Electrochem.*, 2022, 101096.
6 P. A. Defnet and B. Zhang, *ChemElectroChem*, 2020, **7**, 252–259.
7 J. E. Dick, C. Renault, B.-K. Kim and A. J. Bard, *Angew. Chem. Int. Ed.*, 2014, **53**, 11859–11862.
8 F.-R. F. Fan and A. J. Bard, *Nano Lett.*, 2008, **8**, 1746–1749.
9 F. Ben Trad, V. Wieczny, J. Delacotte, M. Morel, M. Guille-Collignon, S. Arbault, F. Lemaître, N. Sojic, E. Labbé and O. Buriez, *Anal. Chem.*, 2022, **94**, 1686–1696.
10 A. Zanut, A. Fiorani, S. Canola, T. Saito, N. Ziebart, S. Rapino, S. Rebeccani, A. Barbon, T. Irie, H.-P. Josel, F. Negri, M. Marcaccio, M. Windfuhr, K. Imai, G. Valenti and F. Paolucci, *Nat. Commun.*, 2020, **11**, 2668.
11 W. Guo, P. Zhou, L. Sun, H. Ding and B. Su, *Angew. Chem. Int. Ed.*, 2021, **60**, 2089–2093.
12 M. Sentic, F. Virgilio, A. Zanut, D. Manojlovic, S. Arbault, M. Tormen, N. Sojic and P. Ugo, *Anal. Bioanal. Chem.*, 2016, **408**, 7085–7094.
13 A. G. Theakstone, E. H. Doeven, X. A. Conlan, L. Dennany and P. S. Francis, *Chem. Commun.*, 2019, **55**, 7081–7084.
14 H. Zhu, D. Jiang and J.-J. Zhu, *Chem. Sci.*, 2021, **12**, 4794–4799.
15 M.-M. Chen, C.-H. Xu, W. Zhao, H.-Y. Chen and J.-J. Xu, *Chem. Commun.*, 2020, **56**, 3413–3416.
16 M. Chen, W. Zhao, M.-J. Zhu, X.-L. Li, C.-H. Xu, H. Chen and J.-J. Xu, *Chem. Sci.*, , DOI:10.1039/c9sc00889f.
17 M. W. Glasscott and J. E. Dick, *J. Phys. Chem. Lett.*, 2020, **11**, 4803–4808.
18 M. W. Glasscott, S. Voci, P. J. Kauffmann, A. I. Chapoval and J. E. Dick, *Langmuir*, 2021, **37**, 2907–2912.
19 Y. B. Vogel, C. W. Evans, M. Belotti, L. Xu, I. C. Russell, L.-J. Yu, A. K. K. Fung, N. S. Hill, N. Darwish, V. R. Gonçales, M. L. Coote, K. Swaminathan Iyer and S. Ciampi, *Nat. Commun.*, 2020, **11**, 6323.
20 H. Ju, G. Lai and F. Yan, in *Immunosensing for Detection of Protein Biomarkers*, eds. H. Ju, G. Lai and F. Yan, Elsevier, 2017, pp. 171–206.
21 A. Chovin, P. Garrigue and N. Sojic, *Electrochim. Acta*, 2004, **49**, 3751–3757.
22 J. Zhang, S. Arbault, N. Sojic and D. Jiang, *Annu. Rev. Anal. Chem.*, 2019, **12**, 275–295.
23 C. Ma, S. Wu, Y. Zhou, H. Wei, J. Zhang, Z. Chen, J. Zhu, Y. Lin and W. Zhu, *Angew. Chem. Int. Ed.*, 2021, **60**, 4907–4914.
24 H. Ding, W. Guo and B. Su, *Angew. Chem. Int. Ed.*, 2020, **59**, 449–456.
25 S. Rebeccani, A. Zanut, C. I. Santo, G. Valenti and F. Paolucci, *Anal. Chem.*, 2022, **94**, 336–348.
26 W. Miao, J.-P. Choi and A. J. Bard, *J. Am. Chem. Soc.*, 2002, **124**, 14478–14485.
27 G. Valenti, S. Scarabino, B. Goudeau, A. Lesch, M. Jović, E. Villani, M. Sentic, S. Rapino, S. Arbault, F. Paolucci and N. Sojic, *J. Am. Chem. Soc.*, 2017, **139**, 16830–16837.
28 A. J. Wilson, K. Marchuk and K. A. Willets, *Nano Lett.*, 2015, **15**, 6110–6115.
29 J. Zhou, G. Ma, Y. Chen, D. Fang, D. Jiang and H. Chen, *Anal. Chem.*, 2015, **87**, 8138–8143.
30 Y. Chen, D. Zhao, J. Fu, X. Gou, D. Jiang, H. Dong and J.-J. Zhu, *Anal. Chem.*, 2019, **91**, 6829–6835.
31 L. Xu, Z. Zhou, C. Zhang, Y. He and B. Su, *Chem. Commun.*, 2014, **50**, 9097–9100.
32 H. Ding, P. Zhou, W. Fu, L. Ding, W. Guo and B. Su, *Angew. Chem. Int. Ed.*, 2021, **60**, 11769–11773.
33 J. Dong, Y. Lu, Y. Xu, F. Chen, J. Yang, Y. Chen and J. Feng, *Nature*, 2021, **596**, 244–249.
34 Y. Ma, C. Colin, J. Descamps, S. Arbault and N. Sojic, *Angew. Chem. Int. Ed.*, 2021, **60**, 18742–18749.
35 M.-J. Zhu, J.-B. Pan, Z.-Q. Wu, X.-Y. Gao, W. Zhao, X.-H. Xia, J.-J. Xu and H.-Y. Chen, *Angew. Chem. Int. Ed.*, 2018, **57**, 4010–4014.
36 S. Voci, B. Goudeau, G. Valenti, A. Lesch, M. Jović, S. Rapino, F. Paolucci, S. Arbault and N. Sojic, *J. Am. Chem. Soc.*, 2018, **140**, 14753–14760.
37 Z. Zhang, C. Ma, Q. Xu and J.-J. Zhu, *Analyst*, 2022, **147**, 2884–2894.
38 Y. Liu, H. Zhang, B. Li, J. Liu, D. Jiang, B. Liu and N. Sojic, *J. Am. Chem. Soc.*, 2021, **143**, 17910–17914.
39 H. Al-Kutubi, S. Voci, L. Rassaei, N. Sojic and K. Mathwig, *Chem. Sci.*, 2018, **9**, 8946–8950.
40 A. Fiorani, D. Han, D. Jiang, D. Fang, F. Paolucci, N. Sojic and G. Valenti, *Chem. Sci.*, 2020, **11**, 10496–10500.
41 B. Li, X. Huang, Y. Lu, Z. Fan, B. Li, D. Jiang, N. Sojic and B. Liu, *Adv. Sci.*, 2022, 2204715.
42 D. Han, B. Goudeau, D. Jiang, D. Fang and N. Sojic, *Anal. Chem.*, 2021, **93**, 1652–1657.

43 H. Gao, W. Han, H. Qi, Q. Gao and C. Zhang, *Anal. Chem.*, 2020, **92**, 8278–8284.
44 C. Ma, M.-X. Wang, H.-F. Wei, S. Wu, J.-R. Zhang, J.-J. Zhu and Z. Chen, *Chem. Commun.*, 2021, **57**, 2168–2171.
45 D. Bruce and M. M. Richter, *Anal. Chem.*, 2002, **74**, 1340–1342.
46 L. Flamigni, A. Barbieri, C. Sabatini, B. Ventura and F. Barigelletti, in *Photochemistry and Photophysics of Coordination Compounds II*, eds. V. Balzani and S. Campagna, Springer, Berlin, Heidelberg, 2007, pp. 143–203.
47 S. Zanarini, M. Felici, G. Valenti, M. Marcaccio, L. Prodi, S. Bonacchi, P. Contreras-Carballada, R. M. Williams, M. C. Feiters, R. J. M. Nolte, L. De Cola and F. Paolucci, *Eur. J. Chem.*, 2011, **17**, 4640–4647.
48 J. M. Fernandez-Hernandez, E. Longhi, R. Cysewski, F. Polo, H.-P. Josel and L. De Cola, *Anal. Chem.*, 2016, **88**, 4174–4178.
49 B. D. Stringer, L. M. Quan, P. J. Barnard, D. J. D. Wilson and C. F. Hogan, *Organometallics*, 2014, **33**, 4860–4872.
50 L. Yu, Z. Huang, Y. Liu and M. Zhou, *J. Organomet. Chem.*, 2012, **718**, 14–21.
51 E. Kerr, E. H. Doeven, G. J. Barbante, T. U. Connell, P. S. Donnelly, D. J. D. Wilson, T. D. Ashton, F. M. Pfeffer and P. S. Francis, *Eur. J. Chem.*, 2015, **21**, 14987–14995.
52 G. J. Barbante, E. H. Doeven, E. Kerr, T. U. Connell, P. S. Donnelly, J. M. White, T. Lópes, S. Laird, D. J. D. Wilson, P. J. Barnard, C. F. Hogan and P. S. Francis, *Eur. J. Chem.*, 2014, **20**, 3322–3332.
53 B. Newman, L. Chen, L. C. Henderson, E. H. Doeven, P. S. Francis and D. J. Hayne, *Front. Chem.*
54 A. Kapturkiewicz, *Anal. Bioanal. Chem.*, 2016, **408**, 7013–7033.
55 H. Li, L. Bouffier, S. Arbault, A. Kuhn, C. F. Hogan and N. Sojic, *Electrochem. commun.*, 2017, **77**, 10–13.
56 M. A. Haghighatbin, S. E. Laird and C. F. Hogan, *Curr. Opin. Electrochem.*, 2018, **7**, 216–223.
57 E. Kerr, E. H. Doeven, G. J. Barbante, C. F. Hogan, D. J. Bower, P. S. Donnelly, T. U. Connell and P. S. Francis, *Chem. Sci.*, 2015, **6**, 472–479.
58 E. Kerr, E. H. Doeven, G. J. Barbante, C. F. Hogan, D. J. Hayne, P. S. Donnelly and P. S. Francis, *Chem. Sci.*, 2016, **7**, 5271–5279.
59 E. H. Doeven, E. M. Zammit, G. J. Barbante, C. F. Hogan, N. W. Barnett and P. S. Francis, *Angew. Chem. Int. Ed.*, 2012, **51**, 4354–4357.
60 E. H. Doeven, G. J. Barbante, E. Kerr, C. F. Hogan, J. A. Endler and P. S. Francis, *Anal. Chem.*, 2014, **86**, 2727–2732.
61 W. Guo, H. Ding, C. Gu, Y. Liu, X. Jiang, B. Su and Y. Shao, *J. Am. Chem. Soc.*, 2018, **140**, 15904–15915.
62 B. D. Muegge and M. M. Richter, *Anal. Chem.*, 2004, **76**, 73–77.
63 S. Voci, R. Duwald, S. Grass, D. J. Hayne, L. Bouffier, P. S. Francis, J. Lacour and N. Sojic, *Chem. Sci.*, 2020, **11**, 4508–4515.
64 E. Kerr, D. J. Hayne, L. C. Soulsby, J. C. Bawden, S. J. Blom, E. H. Doeven, L. C. Henderson, C. F. Hogan and P. S. Francis, *Chem. Sci.*, 2022, **13**, 469–477.
65 B. D. Gomperts and J. M. Fernandez, *Trends Biochem. Sci.*, 1985, **10**, 414–417.
66 S. Watkins, *Curr. Protoc. Cytom.*, 2009, **48**, 12.16.1-12.16.10.
67 M. Sentic, M. Milutinovic, F. Kanoufi, D. Manojlovic, S. Arbault and N. Sojic, *Chem. Sci.*, 2014, **5**, 2568–2572.
68 Y. You, *Curr. Opin. Chem. Biol.*, 2013, **17**, 699–707.
69 G. Zhang, H. Zhang, Y. Gao, R. Tao, L. Xin, J. Yi, F. Li, W. Liu and J. Qiao, *Organometallics*, 2014, **33**, 61–68.
70 Q. Zhao, M. Yu, L. Shi, S. Liu, C. Li, M. Shi, Z. Zhou, C. Huang and F. Li, *Organometallics*, 2010, **29**, 1085–1091.
71 M. R. Schreier, X. Guo, B. Pfund, Y. Okamoto, T. R. Ward, C. Kerzig and O. S. Wenger, *Acc. Chem. Res.*, 2022, **55**, 1290–1300.
72 L. Chen, D. J. Hayne, E. H. Doeven, J. Agugiaro, D. J. D. Wilson, L. C. Henderson, T. U. Connell, Y. H. Nai, R. Alexander, S. Carrara, C. F. Hogan, P. S. Donnelly and P. S. Francis, *Chem. Sci.*, 2019, **10**, 8654–8667.